minerals

MDPI

Article

Chemical and Mineralogical Characterization of Montevive Celestine Mineral

Noemi Ariza-Rodríguez [1,2], Alejandro B. Rodríguez-Navarro [3,*], Mónica Calero de Hoces [1], Jose Manuel Martin [4] and Mario J. Muñoz-Batista [1,*]

[1] Departamento de Ingeniería Química, Universidad de Granada, 18002 Granada, Spain
[2] Canteras Industriales S.L., 18110 Granada, Spain
[3] Departamento de Mineralogía y Petrología, Universidad de Granada, 18002 Granada, Spain
[4] Departamento de Estratigrafía y Paleontología, Universidad de Granada, 18002 Granada, Spain
* Correspondence: anava@ugr.es (A.B.R.-N.); mariomunoz@ugr.es (M.J.M.-B.)

Abstract: The Montevive celestine mineral deposit, set in the Granada Basin in a marine evaporitic uppermost Tortonian–lowermost Messinian sequence, is the largest reserve in Europe of this economically important strontium ore. Currently, the mine has a large amount of tailings resulting from the rejection of a manual dry screening of high-grade celestine mineral. This visual and density screening was carried out in the early days of mining (1954–1973). Concentrating the celestine mineral and increasing the ore recovery rate would reduce mine operation costs and the generation of new tailings, reducing the impact on the environment. In order to define more adequate concentration methods, we have used complementary analytical techniques such as optical (OM) and scanning and transmission electron microscopy (SEM and TEM), energy-dispersive X-rays (EDXs), X-ray fluorescence (XRF), and X-ray diffraction (XRD) to fully characterize the morphology, microstructure, chemistry, and mineralogy of the celestine mineral. The low-grade mineral is made of prismatic celestine crystals that are replacing a matrix of micro sparry calcite. Other minority minerals are strontianite, dolomite, quartz, and clays (kaolinite, paragonite, and illite). There is also a certain amount of iron oxides and hydroxides (mainly magnetite) associated with clays. We showed that the concentration of low-grade celestine mineral can be achieved through a low-cost and eco-friendly method based on grinding and size separation. The coarser fractions (>5 mm) have more celestine (up to 12 percent units higher than the starting unprocessed mineral) due to the selective loss of calcite and minority minerals (quartz, clays, and iron oxides) that are mainly found in the finer fraction (<1 mm). This process can make mine exploitation more sustainable, reducing the generation of residues that negatively impact the environment.

Keywords: celestine; calcite; solid solution; mineral concentration; Rietveld

Citation: Ariza-Rodríguez, N.; Rodríguez-Navarro, A.B.; Calero de Hoces, M.; Martin, J.M.; Muñoz-Batista, M.J. Chemical and Mineralogical Characterization of Montevive Celestine Mineral. *Minerals* **2022**, *12*, 1261. https://doi.org/10.3390/min12101261

Academic Editor: Pura Alfonso

Received: 29 July 2022
Accepted: 1 October 2022
Published: 5 October 2022

1. Introduction

Celestine ($SrSO_4$) is the Sr-rich end-member of the (Sr, Ba) SO_4 solid-solution series with barite ($BaSO_4$) being the Ba-rich end-member [1–5]. Despite being nearly ideal, the (Sr, Ba) SO_4 solid solution shows a marked bimodal composition close to pure or low-Ba celestine and pure or low-Sr barite, being minerals with intermediate composition rarely found in nature [6,7]. Celestine is a relatively common mineral in sedimentary environments, though large economically exploitable deposits are rare [1]. These deposits are commonly associated with coastal marine carbonate and evaporite deposits such as the one studied here in Montevive, located in the middle of the Granada depression, about 11 km SW of the city of Granada, between the towns of Las Gabias, La Malahá, and Alhendin, Spain [8–13]. These massive accumulations of celestine are thought to have formed during diagenesis due to the interaction of Sr-rich high-salinity solutions with carbonate and sulfate minerals [9,10,14–18].

Celestine is an economically important mineral as it is the principal source of strontium, an element recently classified as a critical raw material by the European Union [19]. Strontium is used for the production of pigments, ceramic and special glasses (X-ray safety glass), pyrotechnics, and electronics (semiconductors, permanent magnet) and in metallurgy, among many other industrial applications [20,21].

The Montevive celestine deposit is the largest reserve in Europe of this economically important strontium ore [22]. Even though the mineralogy and geology of the Montevive deposit have been studied in the past [10,16], this project aimed to study the mineralogy of the celestine mineral in more detail using state-of-the-art analytical techniques and instrumentation [23–25]. In particular, this study used complementary analytical techniques such as optical (OM) and scanning and transmission electron microscopy (SEM and TEM), energy-dispersive X-rays (EDXs), X-ray fluorescence (XRF), and X-ray diffraction (XRD) to fully characterize the morphology, microstructure, chemistry, and mineralogy of the celestine ore mineral. Rietveld refinement of X-ray diffraction data was used for quantitative mineral analysis and to study cationic substitution in mineral crystal structures [15,26–30]. Additional techniques such as thermogravimetry (TGA) were used to validate XRF and XRD data [31]. Specifically, TGA allows us to quantify the concentration of carbonate minerals in the sample. These data were used to validate carbonate mineral data obtained by XRF and XRD analysis. Finally, the combination of macroscopic and microscopic techniques allowed us to determine the chemical and mineralogical composition not only of the bulk but also of individual mineral grain [32]. Another important objective of this study was to validate a mineral concentration method based on grinding and size separation.

The mine produces over 200,000 tons of medium- high-grade minerals (80%) per year. High-grade celestine mineral has been traditionally sorted manually or by dry screening, and large amounts of uneconomical low-medium mineral (50%–65%) have been dumped in the mine tailings. To make mine operation more sustainable, it is necessary to process and concentrate this low-grade mineral [33]. In this regard, below, we demonstrate how a low-cost and simple concentration process based on grinding and size separation can improve the grade over a few percent units [34–37].

2. Materials and Methods

2.1. Celestine Ore

The ore body at Montevive consists of well-stratified, mineralized stromatolites. Single stromatolite banks (up to 50 cm thick) exhibit the following succession: (a) at the base, a finely laminated stromatolite (Figure 1A); (b) in the middle, a laminated stromatolite showing molds of small (up to 1 cm in size) prismatic and/or lenticular gypsum crystals displacing the lamination (Figure 1B); and (c) on the top, a more or less distorted stromatolite including molds of former and bigger (up to 10 cm in length) selenite gypsum crystals (Figure 1C). This succession reflects a progressive increase in the salinity of the environment.

According to Martín et al. [10], lamination in the Montevive stromatolites, originally carbonate in composition, is marked by the existence of alternating clear and dark laminae ranging in thickness from 0.05 to 1 mm (Figure 1A). A significant feature in these stromatolites is the presence of abundant, calcified "macrofilaments" (up to 0.1 mm in diameter and several millimeters in length), mostly visible in the clear laminae (Figure 1D) interpreted as cyanobacterial in origin. According to Martín et al. [10], in the Montevive deposit, two types of celestine are found. One variety consists of acicular crystals (0.15 mm long and 0.03 mm wide), largely replacing the micro sparite matrix of the clear laminae. The other variety occurs as first-generation cement (either tabular-prismatic or fibrous-radiating crystals, up to 0.6 mm long), filling in gypsum molds and synsedimentary fractures (desiccation cracks). Later, a sparry calcite cement, with crystals up to several centimeters in size, completes the void infilling. García Veigas et al. [16], however, considered the Montevive stromatolites as gypsified stromatolites, and the "macrofilaments" were thought to be fecal in origin.

According to these authors, the celestine is replacing microcrystalline prismatic gypsum as pseudomorphs.

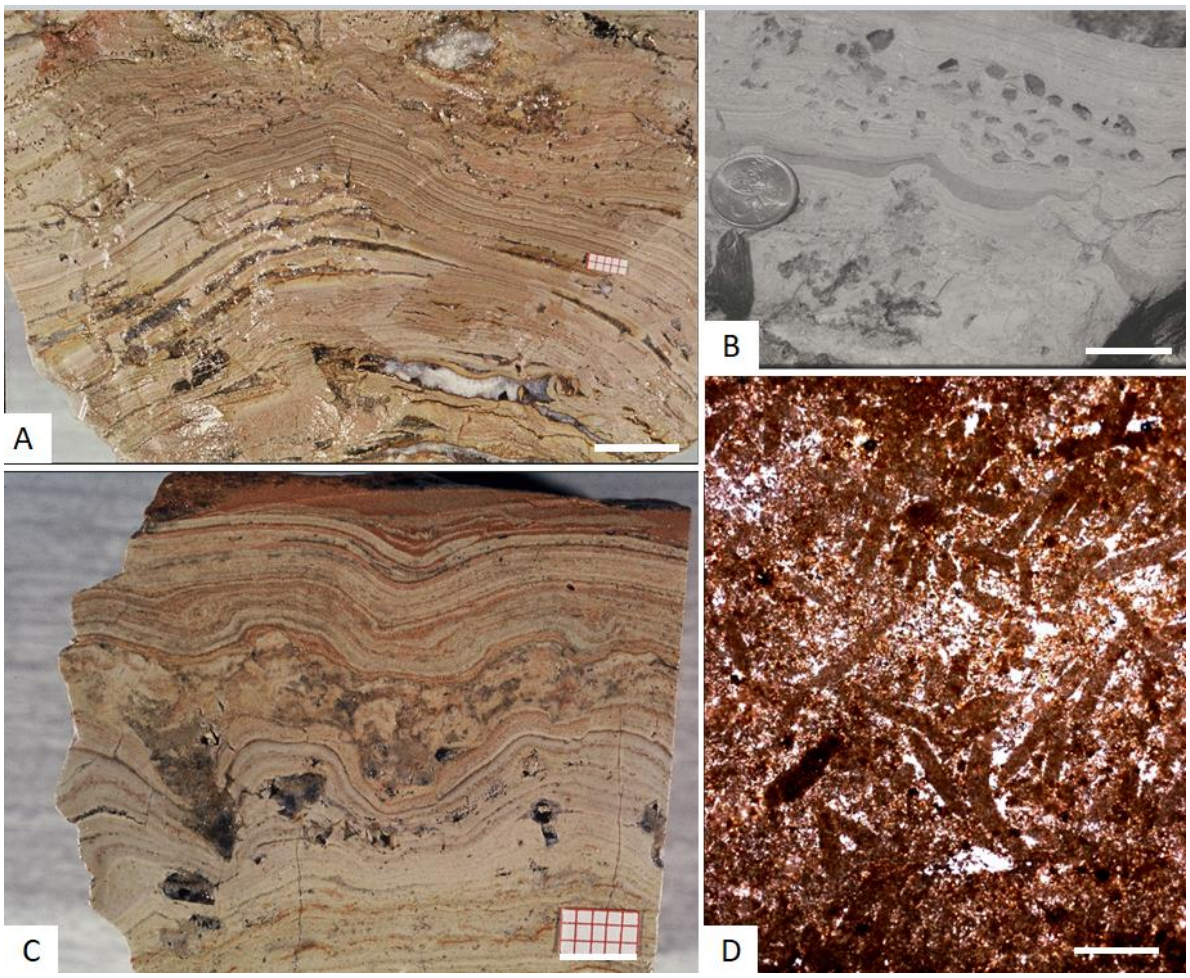

Figure 1. Representative images of Montevive stromatolites. (**A**) Laminated stromatolite. Coarse-crystalline, sparry calcite fills in desiccation cracks parallel to lamination. Scale bar: 1 cm. (**B**) Stromatolite exhibiting molds of small prismatic and lenticular gypsum. Scale bar: 2 cm. (**C**) Stromatolite with a clear selenite mold visible on the left. Scale bar: 5 mm. (**D**) "Macrofilaments" embedded in a micro sparry calcite matrix. Scale bar: 200 μm.

However, in the Montevive ore deposit, the degree of replacement of the former stromatolite by celestine varies from sample to sample, but in all of them, the remaining unreplaced mineral is always a carbonate (calcite and/or dolomite), not gypsum (see Figures 1D and 2). Similar stromatolites have been described extending for kilometers at the margins of the Messinian basins of Sicily and Calabria [18]. They are comparable in size, detailed outcrop morphological features, and internal structure with those of Montevive except that they are not replaced by celestine. They also laterally change to gypsum and salt deposits as in the Granada Basin. They exhibit the same type of "macrofilaments" interpreted, in this study, as bacterial in origin. The Sicilian and Calabrian examples are, in all cases, carbonate stromatolites, not gypsified stromatolites. All in all, these facts suggest that the Montevive stromatolites were originally carbonate stromatolites, not gypsified stromatolites.

2.2. Mineral Samples

The material of the study was provided by the company "Canteras Industriales S.L" that exploits "Mina Aurora" in the Montevive deposit (Figures S1–S3). Representative

celestine mineral samples from the Montevive deposit ranging in purity from 60% to 92% were analyzed. First, about 1000 kg of celestine mineral from selected points from the main mine (E70, E80, E90 and E92) or from the mine tailing (E60 and E69) was collected. From each sampling site, of the total volume of mineral, 1/8 was collected with a loader (L110E Volvo), homogenized, and milled until it reached a particle size of less than 10 mm. About 2 kg of mineral was used for granulometry and optical microscopy analysis. Granulometry of the three main types of samples (E60, E69, and E92) was carried out with an electric sieve shaker (Octagon 2000, Endecotts, London, England) and certified Test Sieves (2000 series, Endecotts, London, England) with 20, 50, 71, 199, 200, 315, 400, and 500 μm and 1, 2, 3.15, 5, and 10 mm sizes (Figure S4**)**. Six fractions of the same mineral sample with different particle sizes were selected and analyzed: 1 (0.1–0.3 mm), 2 (0.3–0.5 mm), 3 (0.5–1.0 mm), 4 (1–2 mm), 5 (2–5 mm), and 6 (5–10 mm) (see Figure S5). After size separation, the fractions were grounded to a particle size of less than 100 μm using a bar mill (1.5 m × 0.25 m steel cylinders). These processed samples were used for chemical and electron microscopy analyses. X-ray fluorescence was performed on a spectrometer used for internal quality control at the mine. Microscopy, thermogravimetric analysis, and X-ray diffraction analysis were carried out with the equipment available at the Departamento de Mineralogía y Petrología and Centro de Instrumentación Científica (Universidad de Granada, Granada, Spain).

2.3. Microscopy

Double-polished thin sections (<30 μm) of the celestine mineral were prepared for optical microscopy. An LZM 1000 microscope (Nikon, Tokyo, Japan) with polarized light was used for imaging and microphotography. A ferricyanide dye was used for carbonate staining. Powdered mineral samples were analyzed by high-resolution scanning electron microscopy (SEM) and energy dispersive X-rays (EDXs) using a Quanta 400 SEM microscope (FEI, USA) operated at 10 kV. Prior to observation, samples were coated with carbon (Hitachi UHS evaporator, Japan). The same samples were also analyzed by transmission electron microscopy (TEM) using a Thermo Fisher TALOS F200X TEM microscope equipped with HAADF and EDX detectors.

2.4. Thermogravimentric Analysis

Mineral samples were analyzed by thermogravimetry (TGA) and differential scanning calorimetry (DSC). About 30 mg of the material was analyzed using a system from METTLER-TOLEDO (mod. TGA/DSC1). A heating rate of 20 °C/min in air was used for registering the TGA and DSC curves. From the TGA curves, the weight loss due to water (25–200 °C) and CO_2 loss due to carbonate thermal decomposition (600–900 °C; $CaCO_3$ >= CO_2 + CaO) were determined. From the weight loss due to carbonate thermal decomposition, the percentage of carbonate minerals in the samples can be calculated [37]. These values were used to validate the carbonate mineral concentrations determined by other methods (XRF and XRD).

2.5. X-ray Fluorescence and X-ray Diffraction

The chemical composition of bulk samples was determined by X-ray fluorescence (XRF) [38–41] using an S2 Ranger Bruker energy-dispersive spectrometer (Bruker-AXS, Ettlingen, Germany) equipped with an X-ray tube with Pd anode and an EDX detector with <155 eV resolution. The system was calibrated using a Cu disk and checked with a glass BAXS-S2.

For the mineralogical and crystallographic characteristics of the mineral, the samples were analyzed by high-resolution X-ray diffraction (XRD) with an Xpert Pro X-ray powder diffractometer (Panalytical, The Netherlands). The samples were measured in reflection mode using copper radiation (from 4 to 120° with 0.017° step size and 100 s integration time per step). Identification of main mineral phases present in the samples (celestine, strontianite, barite, Mg-calcite, dolomite, quartz, kaolinite, illite, and paragonite) was carried out using XpowderX Ver. 2020.01.03 software (www.xpowder.com, accessed on 20

March 2021). Rietveld refinement analyses of XRD profiles were performed using TOPAS 5.0 software (Bruker, Germany) to determine quantitative mineral concentration and unit cell parameters to study ionic substitutions in solid solutions. For peak profile analysis, the fundamental parameters method (FPA) was used [26]. The previously identified mineral phases were defined using the TOPAS mineral database (.str files). Additionally, the clay mineral fraction was analyzed after acid leaching and centrifugation to separate the <2 µm fraction and prepare oriented aggregates to analyze clay basal reflections. Slides were solvated in ethylene glycol at 60 °C to study clay expansion.

3. Results and Discussion

3.1. Optical Microscopy

Optical microscopy was used to analyze the distribution of mineral phases at the millimeter to micrometer scale. Figure 2A displays a view with cross-polarized light showing the calcite matrix in close contact with a massive aggregate of prismatic celestine crystals (from >100 µm to <10 µm in size) that are replacing the calcite matrix (Figure S6). Figure 2B shows the microstructure of a high-grade mineral (E92) made of a massive aggregate of prismatic celestine crystals of larger size (>200 µm). The macrocrystalline celestine corresponds to a first-generation cement, filling in cavities left by desiccation cracks or after larger (up to a few centimeters in size) selenite and/or smaller (a few millimeters in size) prismatic or lenticular gypsum crystal dissolution (Figure 1) [10]. Figure 2C shows a representative view of a thin section of a prewashed medium-grade mineral (E69 observed with plain-polarized light). It has a massive calcite microspar matrix that is stained slightly brownish-black by iron oxides and hydroxides. It has a significant amount of porosity, and there are dolomite microcrystals scattered within the higher porosity zones. Dolomite crystals are stained in blue with ferricyanide.

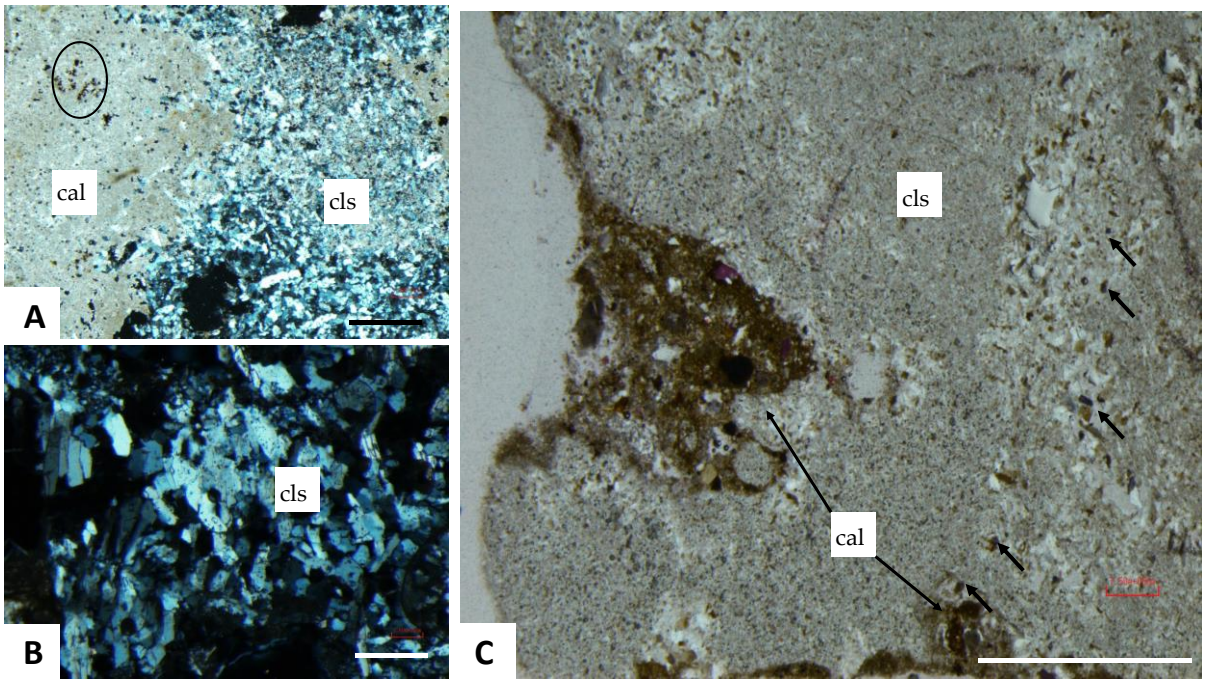

Figure 2. Optical microscopy. (**A**) Representative image with cross-polarized illumination showing micro sparite calcite matrix (cal) and massive celestine (cls) aggregates of prismatic crystals. Circle indicates presence of iron oxides and hydroxides. (**B**) Image of high-grade mineral (E92) made of larger prismatic celestine crystals filling in large synsedimentary voids (desiccation cracks and

evaporite molds). (**C**) Representative image of prewashed medium-grade mineral sample (E69) showing areas with massive calcite (cal) and celestine (cls) aggregates. Calcite matrix demonstrates a darker brown color, whereas celestine has a lighter color. There are disseminated dolomite crystals (arrows) that are stained blue with ferricyanide. Scale bar: 100 μm.

3.2. Granulometry Analysis

Table 1 shows the granulometry of the representative samples of unprocessed mineral (E60, E69, and E92). In sample E60, the predominant fraction is 5–10 mm in diameter, accounting for 32% of the mineral mass. In samples E69 and E92, the predominant fraction is >10 mm, accounting for 29% and 33% of the mineral mass, respectively (see Figure S8 and Table S1). After granulometry, the samples were classified in size fractions (1–6), which were then used to study the effect of grain size on mineral composition.

Table 1. Granulometry analysis of selected samples (E60, E69, and E92), showing accumulated percentage mass (% mass) up to this size range and relative mass fraction (fi) (retained mass divided by total mass).

Size Fraction	Grain Size	Mean Diameter (mm)	E60		E69		E92	
			Fraction	%Mass	Fraction	%Mass	Fraction	%Mass
	>10 mm	>10	0.12	12.07	0.29	29.08	0.33	32.52
6	10–5 mm	7.50	0.32	43.77	0.21	49.93	0.25	57.18
5	5–3 mm	3.51	0.28	83.43	0.20	80.52	0.17	80.88
4	2–1 mm	1.50	0.12	83.43	0.10	80.52	0.07	80.88
3	1.0–0.5 mm	0.75	0.05	88.40	0.07	87.04	0.04	85.11
2	500–315 μm	0.41	0.02	91.57	0.03	91.58	0.02	88.35
1	315–200 μm	0.20	0.04	94.64	0.04	94.73	0.04	91.40
	<100 μm	0.05	0.05	98.81	0.05	98.83	0.07	96.93

3.3. Scanning Electron Microscopy

Scanning electron microscopy was used to analyze the mineral at higher magnification. Figures 3 and S7 show representative SEM images of a low-grade mineral (E60) sample as seen in back-scattering (BS) mode, showing celestine crystals with brighter illumination (high electron density) and carbonate and silicate minerals with lower illumination (lower electron density). There were isolated celestine crystals with a prismatic morphology as well as aggregated celestine crystals that were cemented and/or coated by calcite microcrystals (5–10 μm in size) that showed a characteristic rhombohedral morphology. Furthermore, isolated dolomite microcrystals (<5 μm in size) were found disseminated within the mineral. Kaolinite microcrystals, which demonstrate a characteristic platy shape, were also found associated with the calcite cement. Iron-rich mineral (iron oxides and hydroxides) deposits (<1 μm in size) were also scattered within the mineral (Figure 3E,F). No obvious crystalline morphology was observed for these minerals, even at high magnification. EDX maps showing the distribution of relevant chemical elements (Sr, Ca, Ba, Al, and Fe) are superimposed onto the BS-SEM images shown above (Figure 3D–F). Celestine crystals are highlighted in blue. The EDX spectra of isolated celestine crystals show that most of them have some amount of Ba (in yellow), though it is highly variable. It was also noted that Ba can be concentrated in parallel veins cutting across celestine crystals as shown in Figure 3F. This could be due to an ex-solution process of a Ba-rich phase (barite). There are regions where, because of rough sample topography, no EDX signal was collected due to shadowing, even though there were celestine and calcite crystals clearly distinguished (lower part of Figure 3A,E). Kaolinite crystals were identified by their platy shape and high Si and Al signal.

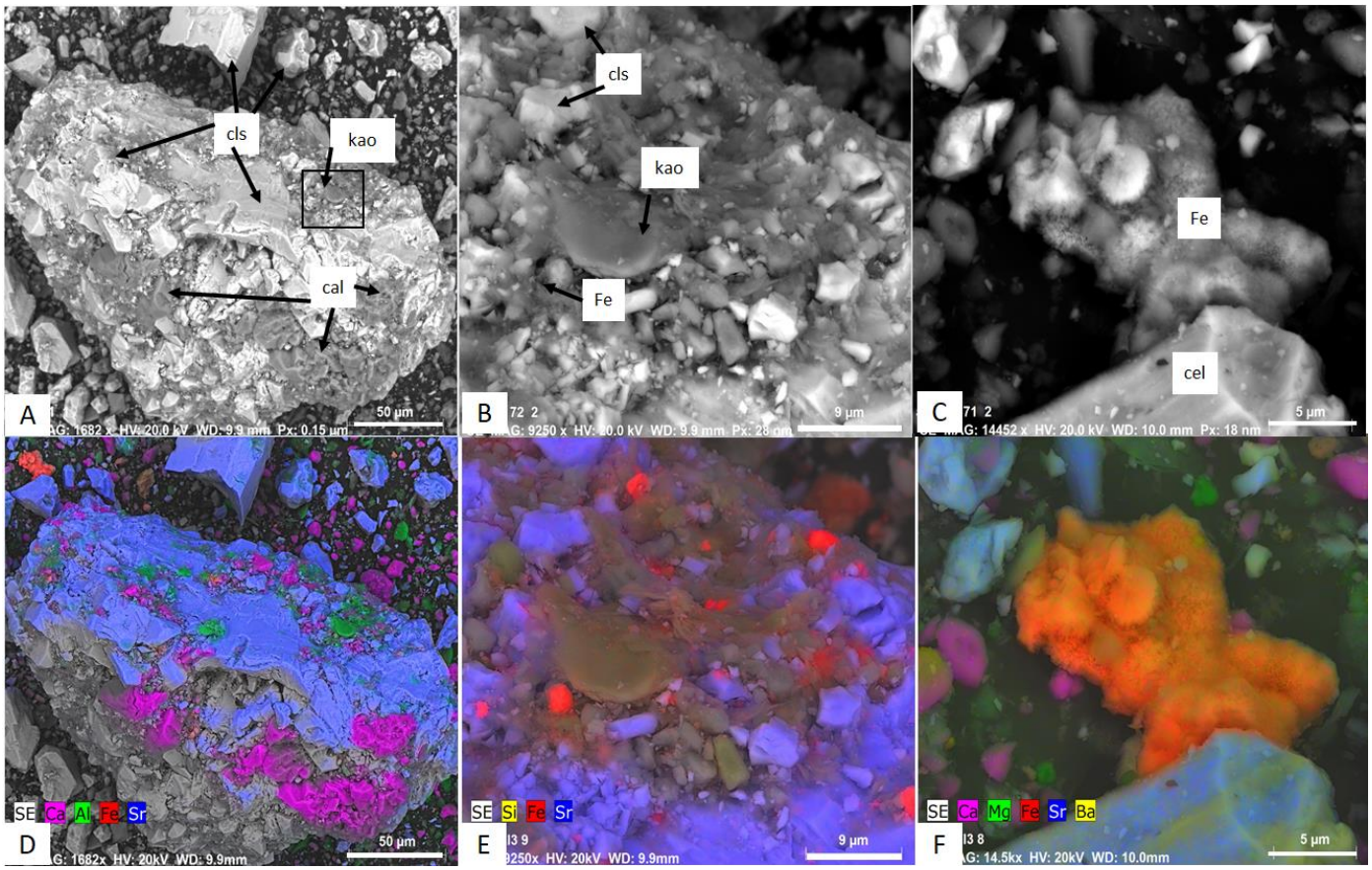

Figure 3. Scanning electron microscopy of E60 sample. (**A**–**C**) Representative images of mineral (BS mode) showing celestine crystals with brighter illumination (electron dense) and calcite and silicate minerals with lower illumination. (**D**–**F**) EDX maps showing distribution of relevant chemical elements (Sr in blue, Ca in purple, Ba in yellow, Al in green, and Fe in red) superimposed onto SEM images shown above. cls: celestine; cal: calcite; kao: kaolinite; Fe: iron oxides and hydroxides.

3.4. Transmission Electron Microscopy

Transmission electron microscopy was used to analyze the mineral in more detail. Figure 4 shows representative TEM images of a low-grade mineral (E60) sample with different mineral assemblages made of celestine and calcite crystals associated with clay mineral particles. EDX maps exhibit the distinct chemical composition of different mineral particles in the assemblage. The clay mineral particles were very thin platy crystals rich in Si and Al, which were identified as kaolinite (as confirmed by their characteristic d-spacings in SAED patterns). The kaolinite crystals were often embedded in a low-density gel-like material rich in Si and Al. There were also isolated iron-rich nanoparticles (<200 nm in size) in the assemblages, which demonstrated well-developed crystal faces and produced well-defined diffraction spots with d-spacings (i.e., 0.252 nm) characteristic of magnetite (Figure 4F).

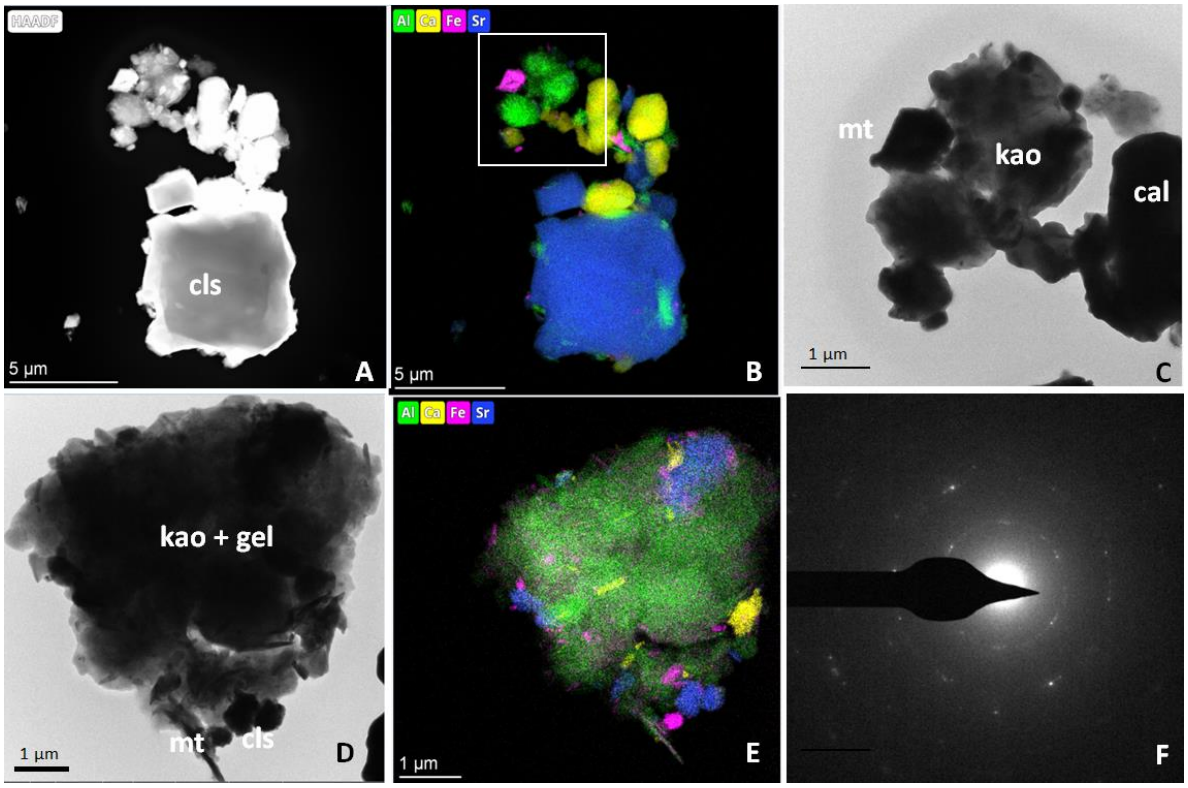

Figure 4. Transmission electron microscopy of E60 sample. Morphology and chemical analysis of mineral assemblages shown in (**A**) and (**D**) studied using different imaging modes: (**A**) STEM mode; (**B**–**E**) EDX maps showing distribution of relevant chemical elements (Sr in blue, Ca in yellow, Al in green, and Fe in pink). (**C**,**D**) Bright field image of mineral assemblage detail (from **B**) and general view (**D**); (**F**) SAED pattern of magnetite nanoparticle. Main mineral phases identified are indicated as follows: cls, celestine; cal, calcite; kao, kaolinite; mt, magnetite. Scale bars: (**A**,**B**): 5 µm; (**C**–**E**): 1 µm.

3.5. X-ray Fluorescence

X-ray fluorescence analysis was used to determine the bulk chemical composition of the mineral samples and how concentration changes with grain size separation (Figure S9). It shows that the main chemical components determined by XRF are $SrSO_4$, $BaSO_4$, $CaCO_3$, $MgCO_3$, SiO_2, Al_2O_3, and Fe_2O_3 as shown in Table 2 and described in more detail hereafter. The main chemical component was $SrSO_4$, with concentrations ranging from 63% to 95%. The second most abundant was $CaCO_3$, from 20% to 46%. SiO_2 and Al_2O_3 accounted for 10% or less. The rest of the components were less than 5%.

On the other hand, the celestine ore was grounded and separated in six different grain size fractions, starting from 1 (0.1–0.3 mm) to 6 (5–10 mm), which all significantly differed in their chemical composition. Generally, there is a gradual increase in $SrSO_4$ concentration with particle size. For instance, in the low- to medium-grade mineral (E60 and E69), $SrSO_4$ increases from 60%–64% in the lowest grain size fraction (EXX_1: 0.2–0.5 mm) to 68%–72% in the coarser size fraction (EXX_6: >5 mm). The increase in $SrSO_4$ concentration is due to the fact that the larger size fractions have a decreased amount of Fe_2O_3-, SiO_2-, and Al_2O_3-rich components. However, this trend is not so evident in the high-grade mineral (E92). Overall, the results suggest that mineral classification and selection of coarser mineral particles (>5 mm), which represents over 45% of the starting mineral weight, is a low-cost and effective method to concentrate low- and medium-grade celestine ore.

Table 2. Chemical composition of representative celestine mineral samples determined by XRF. Suffixes 1 to 6 correspond to fractions of same mineral sample with different particle sizes: 1 (0.1–0.3 mm), 2 (0.3–0.5 mm), 3 (0.5–1.0 mm), 4 (1–2 mm), 5 (2–5 mm), and 6 (5–10 mm).

Sample	$SrSO_4$	$BaSO_4$	Fe_2O_3	SiO_2	Al_2O_3	$CaCO_3$	$MgCO_3$
E60	63.0	1.1	3.1	7.7	3.2	20.6	2.5
E60_1	60.3	1.1	4.1	8.6	3.6	20.6	2.6
E60_2	61.9	1.2	3.7	7.6	3.1	20.6	2.3
E60_3	64.3	1.1	3.6	6.5	2.7	20.1	2.1
E60_4	64.7	1.7	3.1	6.6	2.7	20.5	2.1
E60_5	64.4	1.0	2.8	6.4	2.6	19.5	2.1
E60_6	71.5	1.7	2.4	6.1	2.5	14.4	1.9
E69	70.5	1.2	1.9	5.5	0.0	16.0	2.0
E69_1	64.0	1.2	2.4	6.4	2.6	20.6	3.1
E69_2	62.6	1.3	2.3	6.9	2.8	20.8	3.3
E69_3	63.3	1.1	2.2	6.9	2.8	20.5	3.3
E69_4	64.3	1.1	1.8	5.5	2.3	21.9	3.0
E69_5	68.5	1.2	1.5	3.9	1.6	19.5	2.3
E69_6	67.1	0.9	0.8	2.5	1.0	24.0	1.9
E70	52.2	1.2	0.4	0.9	0.3	46.6	0.9
E80	74.9	0.3	0.7	5.4	0.0	17.3	0.9
E90	95.8	1.9	0.1	0.4	0.3	0.0	0.4
E92	90.7	1.4	0.1	2.2	0.4	2.8	0.7
E92_1	89.8	1.5	0.8	2.5	0.5	3.6	0.9
E92_2	88.2	1.5	0.7	2.6	0.4	4.3	0.8
E92_3	88.9	1.5	0.6	2.4	0.4	3.4	0.8
E92_4	88.7	1.5	0.5	2.1	0.4	3.6	0.7
E92_5	90.4	1.5	0.5	2.3	0.4	3.3	0.6
E92_6	88.4	1.5	0.4	2.9	0.4	5.6	0.5

Correlation Analysis

Pearson correlation analyses for the main chemical components determined by XRF are shown in Table 3. These data provide additional information regarding the chemistry of the mineral and the relationship among chemical components. For instance, there is a strong negative correlation between $SrSO_4$ and $CaCO_3$ ($R = -0.939$; $p < 0.001$) as celestine ($SrSO_4$) is replacing the calcite ($CaCO_3$) matrix. $SrSO_4$ is positively correlated with $BaSO_4$ as Ba is incorporated into celestine, as discussed in the XRD section. SiO_2 and Al_2O_3 are strongly and positively correlated ($R = 0.862$; $p < 0.001$) as they are the main chemical components of clay minerals (kaolinite and paragonite). When plotting SiO_2 versus Al_2O_3, most of the points fall in a straight line except for a few points, which we assume are due to quartz (SiO_2) (see Figure S10). The previous components (SiO_2 and Al_2O_3) are also highly and positively correlated with Fe_2O_3 ($R = 0.909$; $p < 0.001$), indicating that iron oxides and hydroxides are associated with clays. On the other hand, $MgCO_3$, which is part of dolomite, is also highly correlated with SiO_2 and Al_2O_3 and not correlated with $CaCO_3$, indicating that dolomite is associated with clays and not with calcite [42].

Table 3. Correlation analysis between phase determined by XRF. Significant correlations ($p < 0.05$) are in bold type.

	$SrSO_4$	$BaSO_4$	Fe_2O_3	SiO_2	Al_2O_3	$CaCO_3$	$MgCO_3$
$SrSO_4$	1.000	0.590	−0.711	−0.681	−0.699	−0.940	−0.525
$BaSO_4$	0.590	1.000	−0.294	−0.451	−0.198	−0.595	−0.226
Fe_2O_3	−0.711	−0.294	1.000	0.921	0.909	0.454	0.631
SiO_2	−0.681	−0.451	0.921	1.000	0.862	0.413	0.679
Al_2O_3	−0.699	−0.198	0.909	0.862	1.000	0.442	0.702
$CaCO^3$	−0.940	−0.595	0.454	0.413	0.442	1.000	0.287
$MgCO_3$	−0.525	−0.226	0.631	0.679	0.702	0.287	1.000

3.6. X-ray Diffraction

The results of the X-ray diffraction analysis show that the main mineral phases present in the celestine ore are sulfates (celestine), carbonates (calcite, dolomite, and strontianite), and silicates (quartz, kaolinite, paragonite, and illite) as shown in Table 4 and described in more detail hereafter. The concentration of each mineral was determined using Rietveld refinement of XRD data considering the previously identified mineral phases (see SI Figure S11). In addition, Rietveld analysis was used to refine unit cell parameters to study ionic substitutions in main mineral phases (celestine, calcite, and dolomite).

3.6.1. Sulfates

Celestine was the main mineral phase found in the samples, with concentrations ranging from 60% up to 92%. No other sulfate mineral (barite, gypsum, or anhydrite) was detected by XRD. However, XRF and EDX data show a significant concentration of Ba (up to 1.3% from XRF data), which seems mainly incorporated into the celestine as a solid solution. The incorporation of Ba into the celestine structure produced a significant increase in the crystal cell parameters (up to 0.1% in the a-axis). Interestingly, the lattice distortions are greater in the mineral with the highest celestine concentrations (E92), which indicates that the barium content in celestine in these samples is slightly higher. For instance, the estimated Ba content in celestine ranges from 0.4% in the samples with 60% celestine (E60) to 1.7% in the samples with 92% celestine (E92). This was estimated from the unit cell parameters (a-axis) of the Ba-celestine, considering the parameters of pure celestine and barite as end members of the solid solution. EDX maps show that Ba is only associated with celestine through its distribution in some crystals, which is not homogenous. Furthermore, some crystals contain parallel veins, which could be indicative of an ex-solution process of a barium-rich phase (Figure 3F).

3.6.2. Carbonates

Calcite was the main carbonate mineral (up to 57%) that formed part of a massive aggregate of micro sparry calcite crystals that have been partially replaced by celestine (Figure 2). Calcite also occurs as a late, second-generation cement, filling in gypsum-crystal molds, desiccation cracks, and veins, after the first-generation, coarse-crystalline celestine [10]. Subsequently, there is a strong negative correlation between the concentrations of the two mineral phases ($R = -0.940$; $p < 0.001$). It has a low Mg content (<0.8%) as estimated from the calcite unit cell parameters [37]. Dolomite was found in all samples (up to 5.5%) except in the high-grade ones (92% celestine; E92). Another minority carbonate mineral found was strontianite, which showed the highest concentration (up to 3.1%) in the lower-grade mineral (E60).

3.6.3. Silicates

Quartz was present in all mineral samples (up to 5.1%) and was associated with clay minerals (kaolinite, paragonite, and illite). Kaolinite (up to 6.0%), paragonite (up to 4.8%), and illite (<0.5%) were the main clay minerals determined by XRD analysis. Interestingly, in the minority phase, illite was the most abundant clay mineral in the high-grade mineral (92% celestine), whereas kaolinite and paragonite were the dominant phases in the lower-grade ore (60%–80%). All these minerals are commonly found in terrigenous sediments derived from the erosion of the Sierra Nevada mountain range and are transported by rivers into the Granada Basin [10]. The mineralogy of clays was confirmed by the preparation of oriented aggregates showing that paragonite and kaolinite were the main clay minerals in the celestine mineral (Figure 3).

3.6.4. Other Minerals

The results of the XRF analysis show that there was a significant amount of iron oxides (up to 4% in lower-grade mineral), though no iron oxides and hydroxides minerals were detected by XRD analysis. However, optical microscopy and SEM-EDX maps show that

they are Fe-rich mineral particles, whereas the results of the TEM analysis show that they are magnetite. Terrigenous sediments in the Granada Basin typically have a significant amount of iron oxides.

Table 4. Quantitative mineral composition of samples determined by X-ray diffraction Rietveld method.

	Calcite	Celestine	Strontianite	Quartz	Dolomite	Kaolinite	Illite	Paragonite
E60	24.4	59.1	1.8	5.1	0.5	5.8	0.0	2.4
E60_1	27.1	55.7	1.9	5.4	0.2	6.0	0.1	2.7
E60_2	27.3	55.9	1.5	4.5	0.6	6.1	0.0	2.7
E60_3	23.3	60.2	1.6	3.3	1.4	5.2	0.0	2.3
E60_4	23.5	63.0	1.4	4.0	0.7	4.3	0.0	2.4
E60_5	24.8	59.1	2.5	4.2	1.0	4.7	0.0	2.5
E60_6	18.3	67.9	1.8	4.2	0.7	4.4	0.0	1.8
E69	24.2	58.7	1.8	5.1	0.6	6.0	0.0	2.4
E69_1	25.9	54.9	3.1	4.7	4.2	5.0	0.0	2.6
E69_2	24.0	53.9	2.8	4.4	5.6	4.6	0.0	2.4
E69_3	23.9	55.8	2.9	4.2	5.0	4.8	0.0	2.4
E69_4	25.9	59.0	2.2	4.1	4.4	3.9	0.0	2.6
E69_5	21.3	66.1	1.9	3.2	4.2	2.6	0.0	2.1
E69_6	23.2	67.1	0.3	4.2	3.2	1.4	0.0	2.3
E70	57.3	39.3	0.7	1.2	0.4	0.2	0.1	5.7
E80	28.4	67.3	0.7	1.0	1.3	0.2	0.0	2.8
E90	1.8	92.3	0.8	0.5	3.4	0.3	0.0	0.2
E92	3.9	91.9	1.1	0.5	0.0	2.1	0.0	0.4
E92_1	3.6	93.2	0.7	1.2	0.0	1.2	0.0	0.4
E92_2	2.7	94.6	0.2	1.9	0.0	0.2	0.0	0.3
E92_3	3.2	93.0	0.1	3.1	0.0	0.4	0.0	0.3
E92_4	3.8	92.9	0.1	1.9	0.0	0.5	0.6	0.4
E92_5	3.2	93.0	0.1	2.6	0.0	0.4	0.6	0.3
E92_6	4.6	92.4	0.1	2.0		0.4	0.5	0.5

3.6.5. Correlation Analysis

Correlation analyses for the main mineral phases determined by XRD are shown in Table 5. These data provide additional information about the mineralogy of the samples. For instance, there is a strong negative correlation between celestine and calcite as the calcite micritic matrix is replaced by celestine. Calcite strongly correlates with clays but not with dolomite, which indicates that these two carbonates are not associated with each other. Strontianite is strongly and positively correlated with calcite, dolomite, quartz, and clay minerals and negatively correlated with celestine. In particular, strontianite shows the strongest correlation with dolomite, suggesting a common origin. Dolomite and other minority minerals could have a microbial origin [43]. Celestine replacement of the carbonate matrix could be interpreted as a mineral dissolution replacement reaction. When a solution comes into contact with highly soluble chemically reactive minerals (i.e., calcite and gypsum), they start to dissolve, releasing ions that induce the precipitation of less soluble minerals (apatite, celestine, and barite) [6,44]. In the dissolution–replacement reaction, there is some porosity generation that facilitated its progression. In this case, the high porosity of the carbonate matrix should have facilitated the replacement.

Clays (kaolinite and paragonite) are strongly correlated among themselves. Quartz comprises all parts of the finer fraction of the mineral. Another interesting relationship is the strong and positive correlation between iron oxides and the concentration of quartz and clay minerals, particularly kaolinite (R = 0.810; $p < 0.001$). Figure S10 shows the relationship between % Al_2O_3 and % SiO_2 obtained by XRF. This association is confirmed by TEM showing magnetite with kaolinite. The association of iron oxides with clay minerals (kaolinite) suggests a common detrital origin.

Overall, these results are consistent with XRF data, which show a high correlation with XRD data for the main chemical and mineral components (Figure S12). However,

linear regression analysis of XRF and XRD data for some minerals shows that XRF data underestimate the concentration of certain minerals (calcite) (Figure S13) as independently confirmed by TGA (see Table S2 and Figure S14). The later data show that there is a better correlation between the calculated concentrations of carbonate minerals by quantitative XRD Rietveld analysis and TGA data than by XRF and TGA data. Moreover, XRD analysis provides complementary and more detailed information about different minority mineral phases (strontianite, dolomite, and clays) and their chemical associations, which was not possible to obtain from only XRF or EDX data. The results of the TEM analysis confirmed the occurrence of specific clay minerals (kaolinite) and the presence of magnetite nanoparticles, which were associated with clays.

On the other hand, the grinding and size separation processes produced mineral fractions with significantly different mineral compositions. In coarser fractions (e.g., E60_6), there was a gradual loss of calcite, whereas in the more fine-grained minerals (clays), there was a significant enrichment of the ore that increased the concentration of celestine up to 12 percent units (from 55.7% up to 67.9%; E60; Table 4). In high-grade minerals (E92), as also seen by XRF, there was no additional increase in the concentration of celestine, and there was only a small reduction in the amount of clays. Therefore, there is no clear benefit in applying this method to a high-grade mineral.

Table 5. Correlation analysis between phase determined by XRD. Significant correlations ($p < 0.05$) are in bold type.

	Calcite	**Celestine**	**Strontianite**	**Quartz**	**Dolomite**	**Kaolinite**	**Illite**	**Paragonite**
Calcite	1.000	−0.940	0.474	0.384	0.213	0.416	−0.374	0.805
Celestine	−0.940	1.000	−0.711	−0.623	−0.374	−0.674	0.432	−0.840
Strontianite	0.474	−0.711	1.000	0.653	0.611	0.810	−0.444	0.541
Quartz	0.384	−0.623	0.653	1.000	0.259	0.841	−0.211	0.429
Dolomite	0.213	−0.374	0.611	0.259	1.000	0.210	−0.257	0.077
Kaolinite	0.416	−0.674	0.810	0.841	0.210	1.000	−0.370	0.598
Illite	−0.374	0.432	−0.444	−0.211	−0.257	−0.370	1.000	−0.342
Paragonite	0.805	−0.840	0.541	0.429	0.077	0.598	−0.342	1.000

4. Conclusions

Montevive celestine ore is made of prismatic celestine crystals that are replacing a matrix of micro sparry calcite. Other minority minerals are strontianite, dolomite, quartz, and clays (kaolinite, paragonite, and illite). There is also a certain amount of iron oxides and hydroxides (mainly magnetite) associated with clays. This study analyzed the mineralogy of celestine using complementary analytical techniques (XRF, XRD, SEM-EDX, TEM-EDX, and TGA), which provides detailed information about mineral associations and their origin. For instance, XRD Rietveld quantitative analysis provides more detailed information about different minority mineral phases (strontianite, dolomite, and clays) and their chemical associations, which was not possible to obtain from XRF or EDX data alone. TEM analyses confirm the occurrence of specific clay minerals (kaolinite) and the presence of magnetite nanoparticles associated with clays. The combination of different techniques also allowed us to validate the results obtained from other techniques (TGA and XRD for carbonate mineral). These data show that XRD Rietveld quantitative analysis provides a better estimation of the concentration of certain minerals (e.g., calcite) than XRFThis study demonstrated that low- to medium-grade celestine mineral (about 60% celestine), which is currently uneconomical and accumulated in dumps and mine tailings, can be concentrated through a low-cost and eco-friendly method based on grinding and size separation. The coarser fractions (>5 mm) have a greater concentration of celestine (up to 12 percent units more) due to the selective loss of calcite and other minerals (quartz, clays, and iron oxides). This process cannot be applied to high-grade minerals (about 90% celestine) as there is no additional increase in the concentration of celestine. This study can help in the exploitation and enrichment of mineral deposits, reducing the economic cost of extraction while minimizing

the generation of residues that negatively impact the environment. This would, in turn, make the mine operation more sustainable and eco-friendlier. In the near future, other mineral concentration methods (based on high-density media) will be analyzed.

Supplementary Materials: The following supporting information can be downloaded at: https://www.mdpi.com/article/10.3390/min12101261/s1, Figure S1: Sample E70, Figure S2: Sample E 80, Figure S3: Sample E90. Figure S4: Assembly electric vibrator, Figure S5: Gravimetry fractions, Figure S6: Optical microscopy of celestine crystals replacing carbonate, sample E69., Figure S7: Scanning electron microscopy (a) and compositional SEM map of E69 sample (b).,Figure S8: Granulometry results, **% mass$_r$** and **f$_i$** to each diameter (mm) in E60, E69, E92 samples, Figure S9: X-ray fluorescence (representative XRF spectra of one of the samples (E69), Figure S10: Correlation Al_2O_3/SiO_2 obtained in XRF.,Figure S11: Rietveld refinement of X-ray diffraction data used for quantitative mineral analysis, Figure S12: Linear regression model between % $Sr(SO_4)Ba$ obtained by XRF and DRX, Figure S13: Linear regression model between % $CaCO_3$ obtained by XRF and DRX, Figure S14: % $CaCO_3$ by TGA vs. % $CaCO_3$ by XRF or DRX; Table S1: Granulometry results, **% mass$_r$** and **f$_i$** to each diameter (mm) in E60, E69, E92 samples, Table S2: Comparative % $CaCO_3$ by DXR, XRF and TGA methods.

Author Contributions: Conceptualization and methodology: A.B.R.-N., M.J.M.-B., M.C.d.H. and N.A.-R.; software, N.A.-R. and M.J.M.-B.; validation and formal analysis: A.B.R.-N. and N.A.-R.; investigation: A.B.R.-N. and N.A.-R.; writing—original draft preparation, A.B.R.-N., M.J.M.-B. and N.A.-R.; writing—review and editing: A.B.R.-N., M.J.M.-B., N.A.-R., M.C.d.H. and J.M.M.; project administration and funding acquisition: A.B.R.-N. and M.J.M.-B. All authors have read and agreed to the published version of the manuscript.

Funding: This research was funded by Programa Doctorado Industrial PP19.01, UCE PP 2016.05 (Universidad de Granada), and RNM-938 (Junta de Andalucia).

Data Availability Statement: All data is freely available and ccan be requested to the authors.

Acknowledgments: We thank Isabel Sanchez, Rocio Marquez, Cecilia de la Prada, and Miguel Angel Salas (CIC-UGR) for their help with the analyses.

Conflicts of Interest: The authors declare no conflict of interest.

References

1. Nesse, W.D. *Introduction to Mineralogy*; Oxford University Press: New York, NY, USA, 2000.
2. Butler, J.C. Selected Aspects of the Crystal Chemistry of $BaSO_4$, $SrSO_4$ and $PbSO_4$ Selected Aspects of the Crystal Chemistry of $BaSO_4$, $SrSO_4$ and $PbSO_4$. Ph.D. Thesis, Universidad de Ohio, Athens City, OH, USA, 1941.
3. Chang, L.L.Y.; Howie, R.A.; Zussman, J. *Rock-forming Minerals, 5B: Non Silicates*, 2nd. ed.; Longman: London, UK, 1996.
4. Colville, A.A.; Staudhammer, K. A refinement of the structure barite. *Am. Mineral.* **1967**, *52*, 1877–1880.
5. Deer, W.A.; Howie, R.A.; Zussman, J. *An Introduction to the Rock Fonning Minerals*; Wiley Online Library, Ed.; EEUU: New York, NY, USA, 1967. [CrossRef]
6. Forjanes, P.; Astilleros, J.M.; Fernández-Díaz, L. The formation of barite and celestine through the replacement of gypsum. *Minerals* **2020**, *10*, 189. [CrossRef]
7. Hanor, J.S. Frequency distribution of compositions in the barite-celestine series. *Am. Mineral.* **1968**, *53*, 1215–1222.
8. Cohén, Á. Minas y Mineros de Granada (Siglos XIX y XX). Granada, España: Diputación de Granada. 2002. Available online: https://dialnet.unirioja.es/servlet/libro?codigo=86054 (accessed on 4 September 2022).
9. Hanor, J. A model for the origin of large carbonate and evaporite-hosted celestine ($SrSO_4$) deposits. *J. Sediment. Res.* **2004**, *74*, 168–175. [CrossRef]
10. Martin, J.M.; Ortega Huertas, M.; Torres Ruiz, J. Genesis and evolution of strontium deposits of the granada basin (southeastern spain)—Evidence of diagenetic replacement of a stromatolite belt. *Sediment. Geol.* **1984**, *39*, 281–298. [CrossRef]
11. Taberner, C.; Marshall, J.D.; Hendry, J.P.; Pierre, C.; Thirlwall, M.F. Celestine formation, bacterial sulphate reduction and carbonate cementation of eocene reefs and basinal sediments (igualada, NE spain). *Sedimentology* **2002**, *49*, 171–190. [CrossRef]
12. Riding, R.; Braga, J.C.; Martín, J.M.; Sánchez-Almazo, I.M. Mediterranean Messinian Salinity Crisis: Constraints from a coeval marginal basin, Sorbas, southeastern Spain. *Mar. Geol.* **1998**, *146*, 1–20. [CrossRef]
13. Wallace, A.F. Organic interfaces enhance strontium content of marine barite. *Proc. Natl. Acad. Sci. USA* **2019**, *116*, 13161–13162. [CrossRef] [PubMed]

14. Alía, J.M.; Edwards, H.G.M.; López-Andrés, S.; González-Martín, P.; García-Navarro, F.J.; Mansour, H.R. FT-raman study of three synthetic solid solutions formed by orthorhombic sulfates: Celestine-barytes, barytes-anglesite and celestine-anglesite. *Spectrosc. Lett.* **2000**, *33*, 323–336. [CrossRef]
15. Chen, Y.; Huang, E.; Yu, S. High-pressure raman study on the $BaSO_4$-$SrSO_4$ series. *Solid State Commun.* **2009**, *149*, 2050–2052. [CrossRef]
16. García-Veigas, J.; Rosell, L.; Cendón, D.I.; Gibert, L.; Martín, J.M.; Torres-Ruiz, J.; Ortí, F. Large celestine orebodies formed by early-diagenetic replacement of gypsified stromatolites (upper miocene, montevive-escúzar deposit, granada basin, spain). *Ore Geol. Rev.* **2015**, *64*, 187–199. [CrossRef]
17. James, R.W.; Wood, W.A. The crystal structure of barytes, celestine and anglesite. *Proc. R. Soc. Lond.* **1925**, *109*, 598–620.
18. Perri, E.; Gindre-Chanu, L.; Caruso, A.; Cefalà, M.; Scopelliti, G.; Tucker, M. Microbial-mediated pre-salt carbonate deposition during the Messinian salinity crisis (Calcare di Base fm., Southern Italy). *Mar. Pet. Geol.* **2017**, *88*, 235–250. [CrossRef]
19. European Union. *Critical Raw Materials for Strategic Technologies and Sectors in the Eua Foresight Study*; Publications Office of the European Union: Luxemburg, 2020; Available online: https://ec.europa.eu/docsroom/documents/42881 (accessed on 4 September 2022). [CrossRef]
20. Free and Open Patent and Scholary Search. Available online: http://www.lens.org (accessed on 4 September 2022).
21. Ober, J.A. Mineral commodity summaries 2016. In *Mineral Commodity Summaries*; U.S. Geological Survey: Reston, VA, USA, 2016; p. 205.
22. Jiménez-Peñalvarez, J.D. Nieve, oro, sal, Estroncio. Historia de la Minería en Granada. 2008. Available online: https://www.ugr.es/~{}jorgejp/InvestDoc/mineria.pdf (accessed on 4 September 2022).
23. Melgarejo, J.C.; Proenza, J.A.; Galí, S.; Llovet, X. Técnicas de caracterización mineral y su aplicación en exploración y explotación minera. *Boletín De La Soc. Geológica Mex.* **2010**, *62*, 1–23. [CrossRef]
24. Petruk, W. *Applied Mineralogy in the Mining Industry*; Elsevier Science BV: Amsterdam, The Netherlands; New York, NY, USA, 2000.
25. Vassilev, S.V.; Tascón, J.M.D. Methods for characterization of inorganic and mineral matter in coal: A critical overview. *Energy Fuels* **2003**, *17*, 271–281. [CrossRef]
26. Cheary, R.W.; Coelho, A.A.; Cline, J.P. Fundamental parameters line profile fitting in laboratory diffractometers. *J. Res. Natl. Inst. Stand. Technol.* **2004**, *109*, 1–25. [CrossRef] [PubMed]
27. Girard, A.; Stekiel, M.; Spahr, D.; Morgenroth, W.; Wehinger, B.; Milman, V.; Nguyen-Thanh, T.; Mirone, A.; Minelli, A.; Paolasin, L.; et al. Structural, elastic and vibrational properties of celestine, $SrSO_4$, from synchrotron x-ray diffraction, thermal diffuse scattering and raman scattering. *J. Phys. Condens. Matter* **2019**, *31*, 055703. [CrossRef] [PubMed]
28. Rodriguez-Navarro, A.B. XRD2DScan: New software for polycrystalline materials characterization using two-dimensional X-ray diffraction. *J. Appl. Crystallogr.* **2006**, *39*, 905–909. [CrossRef]
29. Rodriguez-Navarro, A.B.; Alvarez-Lloret, P.; Ortega-Huertas, M.; Rodriguez-Gallego, M. Automatic crystal size determination in the micrometer range from spotty X-ray diffraction rings of powder samples. *J. Am. Ceram. Soc.* **2006**, *89*, 2232–2238. [CrossRef]
30. Salazar, S.; Bravo, J.; Castellanos Román, M. Identificación de la Fracción Mineral del Aerosol Atmosférico, en Una Zona Urbana de la Ciudad de México Por Medio de Difracción y Fluorescencia de Rayos-X. *Atmósfera* **2009**, *2*.
31. Conesa Ferrer, J.A. *Curso Básico de Análisis Térmico*; Editorial Club Universiatrio: Alicante, Spain, 2000.
32. Manzaneda Cábala, J.R. Aplicación de Microscopía en el Procesamiento de Minerales Por Flotación. Ph.D. Thesis, University of Lima, Lima, Peru, 2010.
33. Igathinathane, C.; Ulusoy, U.; Pordesimo, L.O. Comparison of particle size distribution of celestine mineral by machine vision ΣVolume approach and mechanical sieving. *Powder Technol.* **2012**, *215*, 137–146. [CrossRef]
34. Ballester, A.; Verdejo, L.F.; Sancho, J. *Metalurgia Extractiva (Volumen 1)*; Síntesis: Madrid, Spain, 2014.
35. Calero de Hoces, M. Aprovechamiento de Recursos Geológicos Andaluces. Concentración de Celestina. Ph.D. Thesis, Universidad de Granada, Granada, Spain, 1994.
36. Garcés de los Fayos Toruner, F. Procedimiento Para Enriquecimiento en Estroncio de Mineral de Celestina. 1986. Available online: https://www.igme.es/PanoramaMinero/Historico/2003_04/estronci03.pdf (accessed on 4 September 2022).
37. Santos, H.; Neumann, R.; Ávila, C. Mineral Quantification with Simultaneous Refinement of Ca-Mg Carbonates Non-Stoichiometry by X-ray Diffraction, Rietveld Method. *Minerals* **2017**, *7*, 164. [CrossRef]
38. Garske, D.; Peacor, D.R. Refinement of the strontium of celestine. *Z. Krist. –Cryst. Mater.* **1965**, *121*, 204.
39. Ball, T.K.; Booth, S.J.; Nickless, E.F.P.; Smith, R.T. Geochemical prospecting for baryte and celestine using a portable radioisotope fluorescence analyzer. *J. Geochem. Explor.* **1979**, *11*, 277–284. [CrossRef]
40. Li, K.; Li, G.; Zhao, G.; Lu, Y.; Shao, K. Method for Simultaneously Detecting Fluorite, Barite and Celestine, Involves Preparing Artificial Standard Material Followed by Preparing Standard Sample, Scanning Standard Sample, Establishing Standard Curve and Detecting Content. Patent CN108051468A, 18 May 2018. Available online: https://patents.google.com/patent/CN108051468A/en (accessed on 4 September 2022).
41. Liu, C.L.; Zhang, L.; Xu, L.J.; Su, Z.M.; Xie, T.P.; Wang, Y.A. Sr speciation in producing $SrCO_3$ with celestine. *Acta Geochim.* **2014**, *33*, 244–247. [CrossRef]
42. López-Quirós, A.; Barbier, M.; Martín, J.M.; Puga-Bernabéu, Á.; Guichet, X. Diagenetic evolution of Tortonian temperate carbonates close to evaporites in the Granada Basin (SE Spain). *Sediment. Geol.* **2016**, *335*, 180–196. [CrossRef]

43. García-del-Cura, M.A.; Sanz-Montero, M.E.; La Iglesia, A.; Ordóñez, S. Carbonate facies and sedimentological model of travertine-tufa quaternary deposits in the Betic Cordillera (SE Spain). In Proceedings of the 27 th IAS Meeting of Sedimentology, Alghero, Italy, 20–23 September 2009; p. 518.
44. Roncal-Herrero, T.; Astilleros, J.M.; Bots, P.; Rodríguez-Blanco, J.D.; Prieto, M.; Benning, L.G.; Fernández-Díaz, L. Reaction pathways and textural aspects of the replacement of anhydrite by calcite at 25 °C. *Am. Mineral.* **2017**, *120*, 1270–1278. [CrossRef]